DOI: 10.1111/cgf.70167

Eurographics Symposium on Rendering 2025
B. Wang and A. Wilkie
(Guest Editors)

COMPUTER GRAPHICS *forum*
Volume 44 (2025), Number 4

A wave-optics BSDF for correlated scatterers

Ruomai Yang   Juhyeon Kim   Adithya Pediredla   Wojciech Jarosz

Dartmouth College

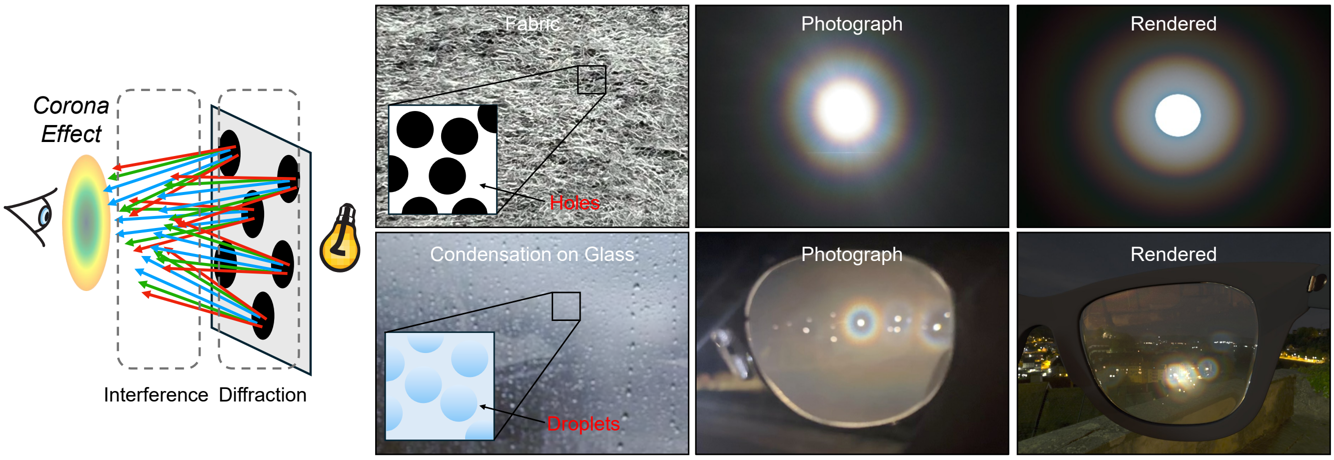

Figure 1: *The corona effect (left) occurs when the diffraction patterns from disordered scatterers interfere with one another. In the real world, this occurs when certain fabrics or condensation on glass (middle-left) are held against bright light sources (middle-right). We propose a novel BSDF that accurately reproduces (right) this wave phenomenon using ray tracing.*

Abstract

We present a wave-optics-based BSDF for simulating the corona effect observed when viewing strong light sources through materials such as certain fabrics or glass surfaces with condensation. These visual phenomena arise from the interference of diffraction patterns caused by correlated, disordered arrangements of droplets or pores. Our method leverages the pair correlation function (PCF) to decouple the spatial relationships between scatterers from the diffraction behavior of individual scatterers. This two-level decomposition allows us to derive a physically based BSDF that provides explicit control over both scatterer shape and spatial correlation. We also introduce a practical importance sampling strategy for integrating our BSDF within a Monte Carlo renderer. Our simulation results and real-world comparisons demonstrate that the method can reliably reproduce the characteristics of the corona effects in various real-world diffractive materials.

CCS Concepts

• ***Computing methodologies*** → ***Reflectance modeling;*** *Ray tracing;* • ***Mathematics of computing*** → *Stochastic processes;*

1. Introduction

Many optical effects observed in everyday life—such as the colorful glints in animal fur and surface scratches, or the multi-colored reflections on thin films and periodic microstructures—cannot be explained by geometric optics alone. Instead, these phenomena arise from the wave nature of light. Over the years, numerous wave-optics appearance models have been developed to simulate such materials, and significant progress has been made in modeling light transport that accounts for wave effects. Together, these advances have enabled impressively realistic renderings.

Despite this progress, rendering materials with disordered yet correlated microstructures remains challenging—particularly for materials composed of randomly positioned, non-overlapping scatterers. Examples include (Fig. 1) glass or mirrors with water condensation, and fabrics or cloth, where complex fiber crossings form random pores. When illuminated by strong directional light, these materials exhibit a characteristic *corona* effect: concentric diffraction rings surrounding the light source. This effect results from the interference of light diffracted by spatially correlated scatterers, as illustrated on the left side of Fig. 1. While the term "corona" typically refers to the diffraction of sunlight by atmospheric particles, similar optical behavior occurs when disordered scatterers—such as apertures or droplets—form a monolayer on a surface.

Such materials fall outside the scope of existing models, which generally assume regular or uncorrelated microstructures. This highlights the need for new approaches to render materials composed of correlated but disordered scatterers. Among prior works, Stam [Sta99] and Dhillon et al. [DTS*14] are most relevant, as they simulate diffraction from structured microsurfaces with repeated bumps. Their formulations, however, are based on height-field representations and assume either periodic or simple Poisson distributions, making them unsuitable for modeling dense, non-overlapping apertures or droplets.

In this work, we present a BSDF model for materials characterized by a layer of disordered, non-overlapping scatterers that produce the corona effect. Our approach builds on prior work in optics [GGB12; LC94; LML20], extending it in several important ways to make it practical for visual simulation. We model the scatterers as a non-overlapping hard-disk system, with their spatial distribution described analytically using pair correlation functions (PCFs). This formulation decouples the spatial relationships between scatterers from the diffraction behavior of individual ones, enabling independent control over both scatterer shape and spatial correlation. We further extend the model to support mixtures of different scatterer types, allowing for more realistic and general representations of natural materials. Additionally, we factorize these effects in a way that makes importance sampling (and multiple importance sampling [VG95]) practical, improving both rendering efficiency and visual quality. Finally, we validate our method against real-world photographs, demonstrating the effectiveness and reliability of our BSDF model in reproducing the corona effect.

2. Previous work

Wave optics in rendering. Wave-optics theory has been widely used in computer graphics to develop analytical appearance models for a variety of materials. Pioneering works by He et al. [HTSG91] and Nayar [Nay91] applied Kirchhoff theory to model light reflection from rough, isotropic surfaces. Stam [Sta99] extended this framework to anisotropic surfaces, accounting for both randomly distributed and periodic height bumps. Later, Oh et al. [OKG*10] and Cuypers et al. [CHB*12] introduced deferred diffraction models using negative radiance, which allowed interference effects to be handled even after multiple bounces. Subsequent research has produced more accurate and efficient appearance models for various microstructures, including structural color from periodic surfaces [DTS*14; TG17], iridescene in thin films [BB17; IA00], and diffraction from surface scratches [VWH18; WVJH17; YHW*18], fur [XWH*23; XWM*20], and feathers [YWW*24]. Yu et al. [YXW*23] recently introduced a full-wave solver to model diffraction from explicit microgeometry, while Steinberg et al. [SRB*24] presented a technique for capturing diffraction effects from macroscopic mesh structures. Wave optics-based scattering models have also been used for volumetric media, from rainbows [SML*12], to Lorenz-Mie scattering [FCJ07] and beyond [GJZ21]. More recently, Xia et al. [XWM23] simulated Quetelet patterns by considering how path differences from discrete particles like dust lead to colorful effects via diffraction and interference.

All of these methods, however, are limited in their ability to simulate the corona effect caused by disordered, non-overlapping apertures or droplets, such as those found in fabric or in water condensation on glass.

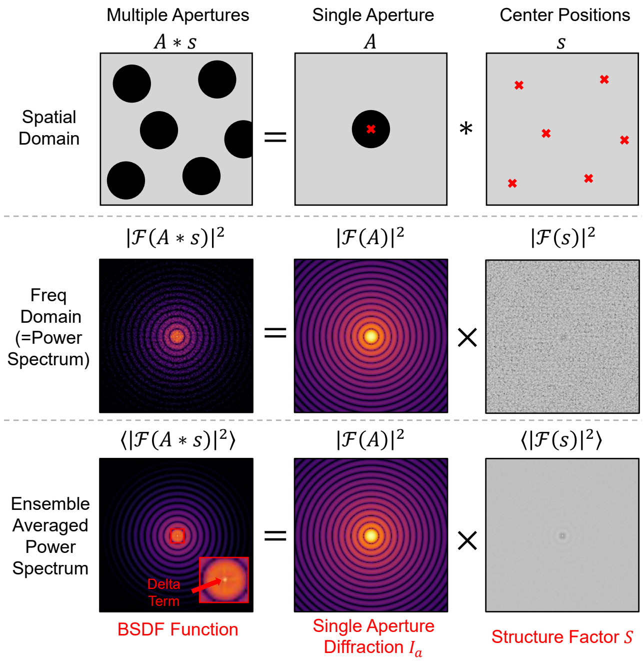

Figure 2: *Our BSDF models scattering from a collection of apertures (top left). In the spatial domain (top row), this collection can be viewed as an aggregate aperture formed by convolving a single aperture shape A with a set of center positions s. Diffraction from this aggregate is computed via a Fourier transform. In the frequency domain (second row), this convolution becomes the product of the single-aperture diffraction pattern I_a and the structure factor S. When s is drawn from a stochastic point process, S is equivalent to the expected power spectrum.*

Corona effect studied in optics. To address this challenge, we draw inspiration from the optics literature, where corona effects have been studied extensively in the context of disordered monolayers of scatterers [GGB12; LC94; LDI00; LML20]. These studies model the phenomenon as a collection of basic scatterers that generate diffraction patterns, and use pair correlation functions to capture the statistical interference between multiple scatterers. *Babinet's principle* [CLV05; vdHul81] is often employed to relate diffraction from apertures to that from particles, while some works use more accurate models based on Lorentz-Mie theory.

Our contribution lies in translating and extending these physical insights into a practical BSDF model suitable for rendering. While prior BSDF models have addressed diffraction from surfaces with random, periodic, or explicitly structured microgeometry, our work considers a unique class of materials formed by a layer of disordered, non-overlapping scatterers.

3. Overview

Our goal is to express the aggregate BSDF for a layer of disordered non-overlapping scatterers. The key point of our method is the decomposition of the BSDF $f_r(\omega_\mathrm{i}, \omega_\mathrm{o})$ into two parts, the diffraction pattern from a single scatterer I_a, and a term that accounts for the correlation/interference within the distribution of scatterers, sometimes called the *structure factor* S,

$$f_r(\omega_\mathrm{i}, \omega_\mathrm{o}) \propto I_a(\omega_\mathrm{i}, \omega_\mathrm{o}) S(\omega_\mathrm{i}, \omega_\mathrm{o}) \tag{1}$$

where $\omega_\mathrm{i}, \omega_\mathrm{o}$ are the incident and outgoing directions. We visualize this decomposition in Fig. 2, and summarize our notation in Table 1 and Fig. 3. In the following sections, we will derive this relationship by combining concepts from Fourier optics (Secs. 4.1 and 4.2) and stochastic point processes (Sec. 4.3) to consider the ensemble-averaged diffraction through a stochastic arrangement of apertures (Sec. 5). We then form a complete BSDF model (Sec. 6) with appropriate handling of the bright delta term in Fig. 2 and scattering from the substrate material, and then propose a practical tabulation approach to evaluate and importance sample the BSDF in a Monte Carlo renderer (Sec. 7).

4. Preliminaries

4.1. Diffraction from a single elementary aperture

In our model, the surface consists of a collection of scatterers. For now, we assume each scatterer is an aperture, and that scattering arises due to diffraction (in Sec. 6.2 we discuss how this can be generalized to particle-like scatterers).

The *Fraunhofer diffraction formula* [Goo17] allows us to express the far-field electric field $[\mathrm{V\,m^{-1}}]$ from a single elementary aperture in terms of the two-dimensional Fourier transform, $\mathcal{F}$, of the aperture function $A(\mathbf{x})$:

$$\mathbf{E}_a(\mathbf{k}) = \alpha \int_{\mathbb{R}^2} A(\mathbf{x}) \mathrm{e}^{-\imath \tilde{\mathbf{k}} \cdot \mathbf{x}} \mathrm{d}\mathbf{x} = \alpha \mathcal{F}\{A(\mathbf{x})\}(\tilde{\mathbf{k}}), \tag{2}$$

where $\mathbf{k} := \mathbf{k}_\mathrm{o} - \mathbf{k}_\mathrm{i} = (\mathbf{k}_x, \mathbf{k}_y, \mathbf{k}_z)$ is the difference between the outgoing wave vector $\mathbf{k}_\mathrm{o} = k_\mathrm{o}\omega_\mathrm{o}$ and the incident wave vector $\mathbf{k}_\mathrm{i} = -k_\mathrm{i}\omega_\mathrm{i}$, and $\tilde{\mathbf{k}} := (\mathbf{k}_x, \mathbf{k}_y)$ is the projection of $\mathbf{k}$ onto the xy plane (Fig. 3). Here, $\imath$ is the imaginary unit, and $\alpha = \frac{\eta E_0 \cos\theta_\mathrm{i} \mathrm{e}^{\imath k_\mathrm{o} R_\mathrm{o}}}{\imath \lambda R_\mathrm{o}}$ is a scaling factor that depends on the wavelength λ, refractive index η, incident angle θ_i and the distance R_o to the observer.

Table 1: *Notation used throughout the paper. See also Fig. 3*

Symbol	Definition
A	Aperture function
a	Radius of aperture or scatterer
F_a, F_r	Area fraction of bounding aperture or real scatterer
$\omega_\mathrm{i}, \omega_\mathrm{o}$	Unit-length incident and outgoing directions
$\theta_\mathrm{i}, \theta_\mathrm{o}$	Incident and outgoing angles
$\mathbf{d}$	Outgoing-incident direction difference $(\omega_\mathrm{o} - \omega_\mathrm{i})$
$d = \lvert\mathbf{d}\rvert$	Length of a vector quantity
$\mathbf{k}_\mathrm{i}, \mathbf{k}_\mathrm{o}$	Incident $(k_\mathrm{i}\omega_\mathrm{i})$ and outgoing $(k_\mathrm{o}\omega_\mathrm{o})$ wave vectors
$\mathbf{k}; \tilde{\mathbf{k}}$	Wave vector difference $(\mathbf{k}_\mathrm{o} - \mathbf{k}_\mathrm{i})$; $\mathbf{k}$ projected onto xy
$\lambda, \lambda_0, \hat{\lambda}$	Incident, reference, and relative (λ_0/λ) wavelengths
η	Refractive index
$\mathbf{E}_a(\mathbf{k}), I_a(\mathbf{k})$	Electric field and irradiance at $\mathbf{k}$ from an aperture a
$s(\mathbf{x})$	Stochastic point process realization evaluated at $\mathbf{x}$
ρ_0	First-order density of s
$\mathcal{F}\{A(\mathbf{x})\}(\tilde{\mathbf{k}})$	Fourier transform of A evaluated at $\tilde{\mathbf{k}}$
$\langle \mathcal{P}_s(\tilde{\mathbf{k}}) \rangle$	Ensemble-averaged power spectrum of s
$g(\mathbf{r}), g(r)$	2D and 1D radial pair correlation function of $s(\mathbf{x})$
$S(\mathbf{k}), S(\tilde{k}), S(\tilde{k})'$	Structure factor: 2D, 1D radial (with, without) delta
J_n	Bessel functions of the first kind

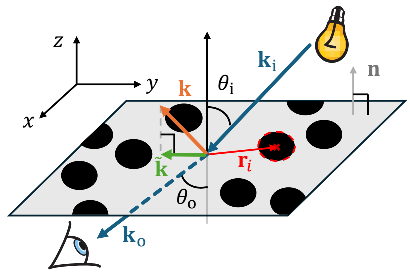

Figure 3: *The primary quantities of our BSDF model in the local coordinate system of a shade point. Refer also to Table 1.*

Up to a scale factor dependent on the material's permittivity, the irradiance $[\mathrm{W\,m^{-2}}]$ is proportional to the squared amplitude of the electric field:

$$I_a(\mathbf{k}) \propto \mathbf{E}_a(\mathbf{k}) \overline{\mathbf{E}}_a(\mathbf{k}) = \lvert\alpha\rvert^2 \lvert\mathcal{F}\{A(\mathbf{x})\}(\tilde{\mathbf{k}})\rvert^2, \tag{3}$$

where $\overline{\mathbf{E}}$ denotes the complex conjugate. A well-known example is the *Airy-disk* pattern from a circular aperture with radius a, which gives $I_a(\mathbf{k}) \propto (2J_1(x)/x)^2$, where $x = a\lvert\tilde{\mathbf{k}}\rvert$ and J_1 is the Bessel function of the first kind.

4.2. Diffraction and interference from a collection of apertures

If we have a discrete collection of N apertures, their diffracted fields *interfere* with each other via the complex-valued sum [LC94]:

$$\mathbf{E}(\mathbf{k}) = \sum_{i=1}^{N} \mathbf{E}_i(\mathbf{k})\, \mathrm{e}^{-\imath \tilde{\mathbf{k}} \cdot \mathbf{r}_i}, \tag{4}$$

where $\mathbf{E}_i$ is the electric field (3) from the i-th aperture (located at $\mathbf{r}_i$, assumed to be in the xy plane). The irradiance of this electric field is proportional to its squared magnitude, $I(\mathbf{k}) \propto \mathbf{E}(\mathbf{k})\overline{\mathbf{E}}(\mathbf{k})$. If we assume the apertures are identical, expanding the product and rearranging terms gives

$$I(\mathbf{k}) \propto N I_a(\mathbf{k}) \overbrace{\left(1 + \frac{1}{N} \sum_{j \neq i} \mathrm{e}^{\imath \tilde{\mathbf{k}} \cdot (\mathbf{r}_j - \mathbf{r}_i)}\right)}^{S(\tilde{\mathbf{k}})}, \tag{5}$$

which shows that the irradiance factors into a term due to the single-aperture diffraction I_a and a structure factor term S that accounts for the arrangement of the apertures.

4.3. Stochastic Point Processes

We proceed by assuming that the positions of the apertures are determined by a *stochastic point process*, and we then reason about the *ensemble-averaged* scattered irradiance.

The computer graphics community has a long history [DW85; LD08; SÖA*19; Uli87] of working with stochastic point processes, for tasks ranging from Monte Carlo integration to random placement of objects. We restrict ourselves to *stationary* point processes—that is, processes whose statistics are translation-invariant.

We can denote a realization of a stochastic point process as the sum of Dirac delta functions centered at random point locations $\mathbf{x}_i$:

$$s(\mathbf{x}) := \sum_i \delta(\mathbf{x}-\mathbf{x}_i). \tag{6}$$

The statistics of such a point process can be analyzed in the spatial domain via its product densities. For stationary processes, the first-order density function $\rho^{(1)}(\mathbf{x}) = \langle s(\mathbf{x})\rangle$, where $\langle\cdot\rangle$ denotes the ensemble average over all possible point realizations, becomes a constant ρ_0. The second-order density $\rho^{(2)}(\mathbf{x},\mathbf{y})$—the joint probability density of finding points around both $\mathbf{x}$ and $\mathbf{y}$—becomes a function of the difference $\rho^{(2)}(\mathbf{x}-\mathbf{y}) = \rho^{(2)}(\mathbf{r})$. This is typically given via the *pair correlation function* (PCF):

$$g(\mathbf{r}) := \frac{\rho^{(2)}(\mathbf{r})}{\rho^{(1)}(\mathbf{x})\rho^{(1)}(\mathbf{y})} = \frac{1}{\rho_0^2}\Big\langle \sum_{j\neq i}\delta(\mathbf{r}-(\mathbf{r}_i-\mathbf{r}_j))\Big\rangle, \tag{7}$$

which is the second-order density of the process *relative* to that of the independent (Poisson) point process.

Alternatively, the point process s can be characterized in the frequency domain by its expected power spectrum [HSD13]:

$$\langle \mathcal{P}_s(\tilde{\mathbf{k}})\rangle := \frac{1}{\rho_0}\langle \mathcal{F}\{s(\mathbf{r})\}\overline{\mathcal{F}}\{s(\mathbf{r})\}\rangle = \frac{1}{\rho_0}\Big\langle \Big|\sum_i \mathrm{e}^{-\imath\tilde{\mathbf{k}}\cdot\mathbf{r}_i}\Big|^2\Big\rangle \tag{8}$$

$$= \frac{1}{\rho_0}\Big\langle \sum_{i,j}\mathrm{e}^{\imath\tilde{\mathbf{k}}\cdot(\mathbf{r}_j-\mathbf{r}_i)}\Big\rangle = 1+\frac{1}{\rho_0}\Big\langle \sum_{j\neq i}\mathrm{e}^{\imath\tilde{\mathbf{k}}\cdot(\mathbf{r}_j-\mathbf{r}_i)}\Big\rangle \tag{9}$$

$$= 1+\rho_0\int_{\mathbb{R}^2}\mathrm{e}^{-\imath\tilde{\mathbf{k}}\cdot\mathbf{r}}g(\mathbf{r})\,\mathrm{d}\mathbf{r} \tag{10}$$

Equation (10) links the power spectrum of s to the Fourier transform of the PCF g. If we equate the first-order point density ρ_0 with N, then this is equivalent to the ensemble average of $S(\tilde{\mathbf{k}})$ in Eq. (5).

5. Diffraction from a stochastic aperture process

Having all the pieces in place, we can now reason about the ensemble averaged diffraction from a stochastic collection of apertures.

Comparing Eq. (9) and the structure factor S in Eq. (5) shows that we can obtain the ensemble averaged scattering from a collection of apertures (whose centers are driven by the stochastic point process s) by multiplying the aperture's power spectrum (3) by the expected power spectrum of the point process $\langle\mathcal{P}_s\rangle$:

$$\langle I(\mathbf{k})\rangle \propto \rho_0 I_a(\mathbf{k})\langle\mathcal{P}_s(\tilde{\mathbf{k}})\rangle. \tag{11}$$

For notational simplicity, we will omit explicitly writing the ensemble average $\langle\cdot\rangle$ from now on, which simplifies Eq. (11) back to Eq. (5).

We can also interpret the stochastic collection of apertures as a convolution $A * s$ of a single aperture A with the point distribution s (see Fig. 2), since, by the Fourier convolution theorem, we have:

$$I(\tilde{\mathbf{k}}) \propto |\mathcal{F}\{A*s\}(\tilde{\mathbf{k}})|^2 = |\mathcal{F}\{A\}(\tilde{\mathbf{k}})|^2|\mathcal{F}\{s\}(\tilde{\mathbf{k}})|^2 = I_a(\tilde{\mathbf{k}})S(\tilde{\mathbf{k}}). \tag{12}$$

This reveals that interference across elementary apertures is nothing more than diffraction from an aggregate aperture.

5.1. Separating the delta component

At $\tilde{\mathbf{k}} = \mathbf{0}$ we have the DC peak (see Fig. 2) of the expected power spectrum (equivalently, the integral in Eq. (10) diverges because the process has an infinite number of points and $g(\mathbf{r}) \to 1$ as $|\mathbf{r}| \to \infty$). For numerical calculations, we subtract the delta (DC) component and redefine the structure factor to focus on the scattering contribution, which captures the interference effects,

$$S(\tilde{\mathbf{k}})' = S(\tilde{\mathbf{k}}) - \rho_0\delta(\tilde{\mathbf{k}}) = 1+\rho_0\int_{\mathbb{R}^2}\mathrm{e}^{\imath\tilde{\mathbf{k}}\cdot\mathbf{r}}(g(\mathbf{r})-1)\mathrm{d}\mathbf{r}. \tag{13}$$

Using this, we can rewrite Eq. (11) as the sum of scattered I^* and delta I^δ parts:

$$I(\mathbf{k}) \propto \underbrace{\rho_0 I_a(\mathbf{k})S(\tilde{\mathbf{k}})'}_{I^*(\mathbf{k})} + \underbrace{\rho_0^2 I_a(\mathbf{k})\delta(\tilde{\mathbf{k}})}_{I^\delta(\mathbf{k})}. \tag{14}$$

5.2. Analytic evaluation of the structure factor

Closed-form parametric expressions for the structure factor are known for some common point processes (sometimes exact, and sometimes approximate). Though the apertures in our model can be arbitrarily shaped, our implementation assumes that the centers of the apertures are distributed according to an isotropic *hard disk process* [AKV08; HM13; Ros90] with a bounding circle of radius a to ensure scatterers do not overlap (see Fig. 4). In graphics this is more commonly referred to as the "blue-noise" Poisson-disk process [LD08]. We leverage the well-known *Percus-Yevick* approximation [PY58], which provides an analytic expression for

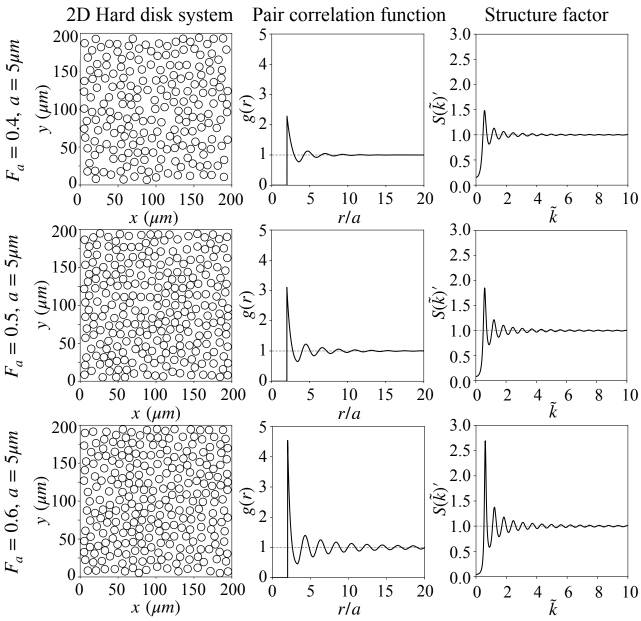

Figure 4: *Sample realizations (left), PCFs (middle), and corresponding structure factors $S(\tilde{k})'$ (right) for a hard disk process with increasing area fraction F_a moving from top to bottom. We plot the PCFs as functions of r/a, where r is distance and a is the disk radius (hence, the PCFs are zero for $r/a < 2$ since disks cannot overlap).*

the power spectrum of this process [Ros90, eqns. 4.4–4.6]:

$$S(\tilde{k} \mid F_a)' = [1 + C(\tilde{k} \mid F_a)]^{-1}, \text{ with} \tag{15}$$

$$C(\tilde{k} \mid F_a) = \frac{4F_a}{1-F_a}\frac{2J_1(2\tilde{k}a)}{2\tilde{k}a} + \frac{4F_a^2 J_0(\tilde{k}a)}{(1-F_a)^2}\frac{2J_1(\tilde{k}a)}{\tilde{k}a} + \left[\frac{F_a^2}{(1-F_a)^2} + \frac{2F_a^3}{(1-F_a)^3}\right]\left[\frac{2J_1(\tilde{k}a)}{\tilde{k}a}\right]^2, \tag{16}$$

where J_n are Bessel functions of the first kind, $F_a = \rho_0 \pi a^2$ is the area fraction, and we use $\tilde{k} := |\tilde{\mathbf{k}}|$ because the process is isotropic.

In Fig. 4, we provide an illustrative example of the PCF and structure factor in a hard disk system to show how the system behaves under different area fractions F_a, over different relative distances (r/a) where $r := |\mathbf{r}|$. The first column shows one realization of circle distributions, while the second and the third column plot the PCF and structure factor respectively, showing increasing oscillatory nature for larger F_a. Note that the PCF remains zero for $r/a \leq 2$ as the particles cannot overlap.

6. A BSDF for correlated apertures

To derive the BSDF, we will first consider a system where all the apertures have the same shape, and later generalize to the case of multiple aperture shapes in the same system.

We decompose the BSDF into three main components (see Fig. 5):

- $f_r^\delta(\omega_\mathrm{i}, \omega_\mathrm{o}, \lambda)$: The delta component, whose irradiance we denoted with $I^\delta(\mathbf{k})$. This captures the specular (or coherent) transmission, where the incident and outgoing directions are identical.
- $f_r^*(\omega_\mathrm{i}, \omega_\mathrm{o}, \lambda)$: The diffraction component caused by scatterers, whose irradiance we denoted with $I^*(\mathbf{k})$.
- $f_r^\circ(\omega_\mathrm{i}, \omega_\mathrm{o}, \lambda)$: The substrate BSDF for light that misses the apertures. We ignore any secondary effects of diffracted light interacting with the substrate BSDF component and assume that these light rays do not interfere.

If we assume each component is normalized, the net BSDF will be

$$w^* f_r^*(\omega_\mathrm{i}, \omega_\mathrm{o}, \lambda) + w^\delta f_r^\delta(\omega_\mathrm{i}, \omega_\mathrm{o}, \lambda) + w^\circ f_r^\circ(\omega_\mathrm{i}, \omega_\mathrm{o}, \lambda), \tag{17}$$

with weights $w^* + w^\delta + w^\circ = 1$ for energy conservation. Our goal is to determine the ratio of the weights $w^* : w^\delta : w^\circ$.

If we define the real area fraction covered by the apertures as $F_\mathrm{r} := \rho_0 |A|$ where $|A|$ is the area of the elementary aperture, then the amount of light that does not interact with apertures is simply $w^\circ = 1 - F_\mathrm{r}$.

For the delta component, we had $I^\delta(\mathbf{k}) = \rho_0^2 I_a(\mathbf{0})\delta(\tilde{\mathbf{k}})$ from Eq. (13) with $I_a(\mathbf{0}) = \alpha^2 |A|^2$ according to Eq. (3), which gives:

$$I^\delta(\mathbf{k}) = \alpha^2 F_\mathrm{r}^2 \delta(\tilde{\mathbf{k}}). \tag{18}$$

Converting to radiance further removes the remaining terms, giving:

$$w^\delta f_r^\delta(\omega_\mathrm{i}, \omega_\mathrm{o}, \lambda) = F_\mathrm{r}^2 \delta(\omega_\mathrm{o}, \omega_\mathrm{i}). \tag{19}$$

Combining this w^δ with our previously defined w°, energy conservation gives the ratio of the components as

$$w^* : w^\delta : w^\circ = F_\mathrm{r} - F_\mathrm{r}^2 : F_\mathrm{r}^2 : 1 - F_\mathrm{r}. \tag{20}$$

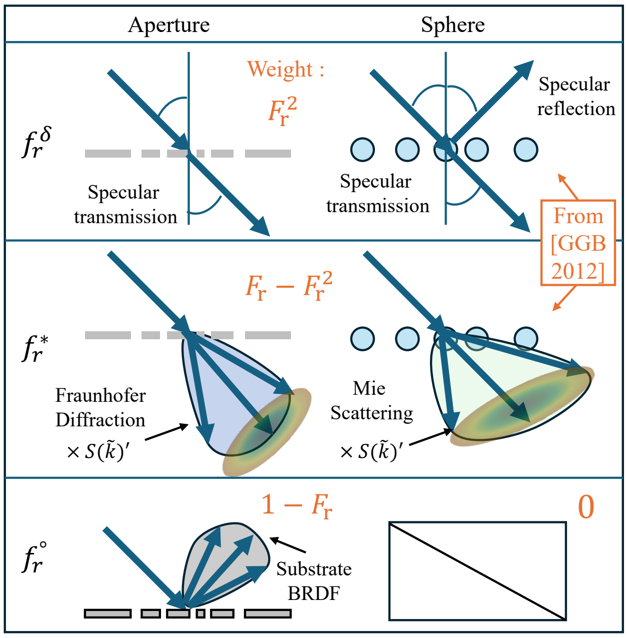

Figure 5: *BSDF components for a layer of apertures (left) and spheres (right). The delta component f_r^δ corresponding to specular transmission (or reflection for spheres), which exists only in specific directions. The diffraction component f_r^* is given by the product of the single-scatterer diffraction I_a—computed using either Fraunhofer diffraction (for apertures) or Mie scattering (for spheres)—and the non-delta structure factor $S(\tilde{k})'$. Finally, f_r° is the BSDF of the substrate material, which is not considered in the sphere case. The weights of each component are indicated in orange: for apertures, they are given by Eq. (20); for spheres, they follow the method of García-Valenzuela et al. [GGB12].*

Note that this only describes the ratio of total energy, while each component's directional distribution should be further evaluated. For $f_r^\delta(\omega_\mathrm{i}, \omega_\mathrm{o}, \lambda)$, only the specular transmission component exists, $f_r^*(\omega_\mathrm{i}, \omega_\mathrm{o}, \lambda)$ should follow Eq. (14)—multiplication of I_a and S', and $f_r^\circ(\omega_\mathrm{i}, \omega_\mathrm{o}, \lambda)$ is determined by the underlying surface material.

6.1. Mixture of Apertures

We now derive the BSDF for a system with multiple aperture shapes. For simplicity, we assume all apertures share the same bounding circle radius. We consider M different aperture types, with $\rho_m = N_m$ apertures of shape A_m distributed per unit area. The total number of apertures is $N = \sum_{m=1}^{M} N_m$. We can then define $P(m) = N_m/N$ as the fraction of type m apertures. We can define two types of PCFs.

The same-type PCF for the m-th aperture type, and the cross-type PCF for two different types m and l, are defined similarly to Eq. (7):

$$g_{mm}(\mathbf{r}) = \frac{1}{\rho_m^2}\left\langle \sum_{j \neq i} \delta(\mathbf{r} - (\mathbf{r}_i^m - \mathbf{r}_j^m)) \right\rangle, \tag{21}$$

$$g_{ml}(\mathbf{r}) = \frac{1}{\rho_l \rho_m}\left\langle \sum_{i,j} \delta(\mathbf{r} - (\mathbf{r}_i^m - \mathbf{r}_j^l)) \right\rangle. \tag{22}$$

Note that $j \neq i$ is unnecessary for the cross-type PCF summation since the particles are already of different types.

The corresponding structure factors (which can be written in terms of the original structure factor $S(\tilde{\mathbf{k}})$) are

$$S_{mm}(\tilde{\mathbf{k}}) = 1 + \rho_m \int_{\mathbb{R}^2} e^{-\imath \tilde{\mathbf{k}}\cdot\mathbf{r}} g_{mm}(\mathbf{r})\,\mathrm{d}\mathbf{r} = (S(\tilde{\mathbf{k}}) - 1)P(m) + 1, \quad (23)$$

$$S_{ml}(\tilde{\mathbf{k}}) = \sqrt{\rho_m \rho_l} \int_{\mathbb{R}^2} e^{-\imath \tilde{\mathbf{k}}\cdot\mathbf{r}} g_{ml}(\mathbf{r})\,\mathrm{d}\mathbf{r} = (S(\tilde{\mathbf{k}}) - 1)\sqrt{P(m)P(l)}. \quad (24)$$

The electric field for a mixture of aperture types can be written as

$$\mathbf{E}(\tilde{\mathbf{k}}) = \sum_{m=1}^{M} \sum_{i=1}^{N_m} \mathbf{E}_m(\tilde{\mathbf{k}}) e^{\imath \tilde{\mathbf{k}}\cdot\mathbf{r}_i^m} \quad (25)$$

where $\mathbf{E}_m(\tilde{\mathbf{k}})$ is the electric field from a type-m aperture. The irradiance is then

$$\begin{aligned} I(\tilde{\mathbf{k}}) = &\sum_{m=1}^{M} \left|\mathbf{E}_m(\tilde{\mathbf{k}})\right|^2 \left(\sum_{i=1}^{N_m}\sum_{j=1}^{N_m} e^{\imath \tilde{\mathbf{k}}\cdot(\mathbf{r}_j^m - \mathbf{r}_i^m)}\right) + \\ &\sum_{m=1}^{M}\sum_{l\neq m}^{M} \left|\mathbf{E}_m(\tilde{\mathbf{k}})\overline{\mathbf{E}}_l(\tilde{\mathbf{k}})\right| \left(\sum_{i=1}^{N_m}\sum_{j=1}^{N_l} e^{\imath \tilde{\mathbf{k}}\cdot(\mathbf{r}_j^l - \mathbf{r}_i^m)}\right) \\ = &\sum_{m=1}^{M} N_m I_m(\tilde{\mathbf{k}}) S_{mm}(\tilde{\mathbf{k}}) + \sum_{m=1}^{M}\sum_{l\neq m}^{M} \sqrt{N_m N_l I_m(\tilde{\mathbf{k}}) I_l(\tilde{\mathbf{k}})} S_{ml}(\tilde{\mathbf{k}}) \quad (26) \end{aligned}$$

Like the single-type case, $I(\tilde{\mathbf{k}})$ can be decomposed into delta and scattered components. We omit the derivation and present only the final result. For the delta component:

$$w^\delta f_r^\delta(\omega_\mathrm{i}, \omega_\mathrm{o}, \lambda) = \left(\sum_{m=1}^{M} F_m\right)^2 \delta(\omega_\mathrm{o}, \omega_\mathrm{i}), \quad (27)$$

which matches Eq. (19) if we redefine $F_\mathrm{r} := \sum_{m=1}^{M} F_m$ with $F_m := \rho_m |A_m|$. The ratio of components therefore remains unchanged for the mixture case.

For the diffraction component:

$$\begin{aligned} w^* f_r^*(\omega_\mathrm{i}, \omega_\mathrm{o}, \lambda) = &\frac{\eta^2 \cos(\theta_\mathrm{i})}{\lambda^2 \cos(\theta_\mathrm{o})} \frac{F_a}{\pi a^2} \left(\sum_{m=1}^{M} P(m)\mathcal{F}_m^2\right. \\ &\left. + \sum_{m=1}^{M}\sum_{l=1}^{M} P(m)P(l)\mathcal{F}_m\mathcal{F}_l(S(\tilde{\mathbf{k}})' - 1)\right) \quad (28) \end{aligned}$$

where $\mathcal{F}_m := |\mathcal{F}\{A_m\}(\tilde{\mathbf{k}})|$. Fig. 10 shows a visual comparison between the single and mixed aperture cases.

6.2. Spherical scatterers

In addition to apertures, we would also like to model the scattering from scatterers like condensation droplets on glass. According to *Babinet's principle* [BH83; vdHul81], the diffraction pattern from a flat opaque object is identical to that from a hole of the same size and shape. Thus, by approximating particles as opaque disks [CLV05; LC94], we can directly use the aperture-based diffraction results, leading to the same BSDF formulation.

For greater accuracy, one can use Mie theory to model scattering from monolayers of spherical particles [LDI00; LML20; LML21]. Scattering from spheres is more complex than from flat apertures, as multiple scattering between particles can occur. However, if the particle size is much larger than the wavelength, forward scattering dominates and multiple scattering can be neglected—a regime known as the single-scattering approximation (SSA) [LDI00]. Under the SSA, we can reuse Eq. (3) for the particle case, substituting I_a from Mie theory, and obtain an expression analogous to Eq. (5). Fig. 6 compares f_r^* computed using Fraunhofer diffraction and Mie theory for various particle radii at a wavelength of $\lambda = 0.55\,\mu\mathrm{m}$. For large particles, Mie theory converges to Fraunhofer diffraction, but in general, the results differ. While Mie theory is more accurate, it is computationally expensive for large particles and I_a depends on $\mathbf{k}_\mathrm{o} \cdot \mathbf{k}_\mathrm{i}$ rather than $\tilde{\mathbf{k}}$, complicating the evaluation. We allow the user to choose between the flat approximation or Mie theory based on their accuracy and performance needs.

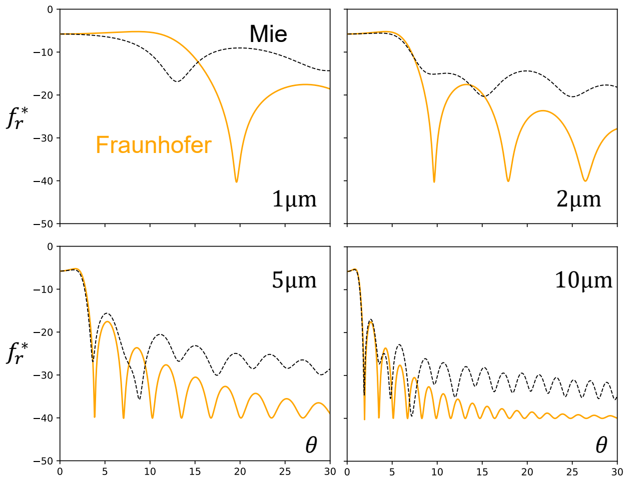

Figure 6: *Fraunhofer diffraction vs. Mie scattering for particle radii $a = 1, 2, 5, 10\,\mu\mathrm{m}$ at wavelength $\lambda = 0.55\,\mu\mathrm{m}$. The area fraction is fixed at $F_a = 0.3$, ω_i is set to the z axis, and θ denotes the angle between ω_i and ω_o. The models produce different results in general, but converge for large radii.*

Determining the ratio of the delta (specular) and diffraction components requires more care for particles than for apertures (Fig. 5). Using the naive area fraction $F_a = \rho_0 \pi a^2$, where a is the sphere radius, is incorrect because a single particle effectively blocks twice its geometric cross section—a phenomenon known as the *extinction paradox* [Bri49; BSC11]. Instead, we follow the heuristic approach of García-Valenzuela et al. [GGB12] to determine the correct ratio between delta and diffraction components.

For simplicity, we treat the particle monolayer as a separate layer above the substrate, setting $f_r^\circ = 0$. Any inter-reflections between the substrate and the particle layer are handled by the ray tracing step, not by the BSDF itself.

7. Evaluating and sampling the BSDF

For practical Monte Carlo rendering, we require efficient evaluation and sampling of our BSDF. Prior work [DTS*14; TG17] has

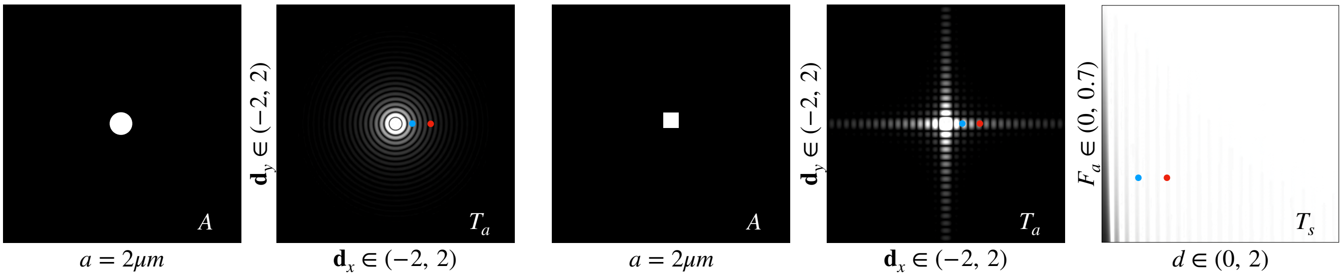

Figure 7: *We precompute textures T_a (images 2 and 4) for the diffraction from a desired aperture shape A (image 1: circle and 3: square). We also precompute a single structure factor texture T_s (far right) for a range of area fractions $F_a \in (0, 0.7)$. During rendering, we evaluate the BSDF by querying (red and blue points) the aperture and structure factor textures based on the incident ω_i and outgoing ω_o directions, wavelength λ, area fraction F_a, and aperture scaling.*

successfully leveraged precomputed tabulations for this purpose. Unfortunately, our full BSDF is a function of many parameters (incoming ω_i and outgoing ω_o directions, wavelength λ, aperture shape A and radius a, and packing fraction F_a). So, while possible, naive tabulation would be expensive, high-dimensional, and inflexible.

Instead, we leverage the separability of the scatterers and their spatial correlations to implement an efficient BSDF for Monte Carlo rendering that uses more modest tabulation while allowing parameter control without retabulation. We also implemented a more naive but higher-dimensional tabulation approach to validate our method.

7.1. BSDF evaluation

We precompute two 2D textures to allow us to efficiently evaluate and sample the BSDF without computing Fourier transforms and structure factors at runtime. For each aperture shape A, we tabulate an aperture diffraction texture $T_a(\mathbf{d}) := |A|^{-1}|\mathcal{F}\{A\}(2\pi/\lambda_0\mathbf{d})|^2\lambda_0^{-2}$ over the range of all possible projected difference vectors $\mathbf{d} := (\omega_\text{o} - \omega_\text{i})_{xy} \in (-2,2)^2$. For the structure factor, we perform a one-time tabulation of Eq. (15) into a texture T_s across all valid values $d := |\mathbf{d}| \in (0,2)$ and $F_a \in (0, 0.7)$. We precompute both textures with respect to a single *reference* wavelength $\lambda_0 = 0.35\,\mu\text{m}$ (the shortest in the visible spectrum) to ensure high-frequency components are captured and remain valid for longer wavelengths during lookup. For arbitrary λ, we can reuse both textures with coordinates scaled by $\hat{\lambda} := \lambda_0/\lambda$. Fig. 7 shows examples of T_a for a circular aperture with a radius of $a = 2\,\mu\text{m}$, a square aperture inscribed within that circle, and the single texture T_s that we use for any aperture shape.

To evaluate the diffraction component $f_r^*(\omega_\text{i}, \omega_\text{o}, \lambda)$, we compute the projected difference vector $\mathbf{d}$ and fetch $T_a(\hat{\lambda}\mathbf{d})$ (marked as the red dot in Fig. 7). Then, given a desired area fraction (e.g., $F_a = 0.5$), we look up the structure factor at the corresponding location $T_s(\hat{\lambda}\,|\mathbf{d}|, F_a)$ (also marked in red). Scaling the lookup coordinates by some additionally factor q (blue dots in Fig. 7) allows us to scale the entire aperture system. The final result is

$$f_r^*(\omega_\text{i}, \omega_\text{o}, \lambda) = \frac{\cos\theta_\text{i}}{\cos\theta_\text{o}}\, T_a(\hat{\lambda}\, q\, \mathbf{d})\, T_s(\hat{\lambda}\, q\, |\mathbf{d}|, F_a)\, \frac{(\eta\hat{\lambda} q)^2}{1 - F_\text{r}}, \tag{29}$$

where the squared factors account for index-of-refraction, wavelength, and system-wide scaling.

7.2. Importance sampling

To importance sample $f_r^*(\omega_\text{i}, \omega_\text{o}, \lambda)$, we perform MIS between the T_a and T_s textures (e.g., the second and fifth images in Fig. 7). We precompute a piecewise-constant 2D distribution $p_a(\mathbf{d})$ from T_a, and 1D piecewise-constant distributions $p_s(d \mid F_a)$ for each row F_a of T_s. We use $P_s(d \mid F_a)$ to denote the CDF of p_s.

Sampling T_a. Given the incident direction $\omega_\text{i} := (x_\text{i}, y_\text{i}, z_\text{i})$ and wavelength λ, we sample a coordinate $\mathbf{d}$ from p_a, and compute the outgoing direction as

$$\omega_\text{o} = \left(x_\text{o} = x_\text{i} + \frac{\mathbf{d}_x}{\hat{\lambda}},\; y_\text{o} = y_\text{i} + \frac{\mathbf{d}_y}{\hat{\lambda}},\; z_\text{o} = \sqrt{1 - x_\text{o}^2 - y_\text{o}^2}\right). \tag{30}$$

If the resulting values lead to an invalid direction, $x_\text{o}^2 + y_\text{o}^2 > 1$, we discard the sample and return zero. The PDF of ω_o is $p_a(\mathbf{d})$ divided by the Jacobian $|\mathbf{d} \to \omega_\text{o}| = z_\text{o}^{-1}\hat{\lambda}^{-2}$.

Sampling T_s. Given ω_i and F_a, we choose a row of T_s and sample from its CDF P_s to obtain d_sample. For an arbitrary wavelength λ, the valid range for sampling within the row changes. We can still use the same precomputed P_s and avoid generating invalid samples by restricting inverse-CDF sampling to $d_\text{sample} < d_\text{max} := (|(\omega_\text{i})_{xy}| + 1)\hat{\lambda}$. Given d_sample, we construct the projected difference vector $\mathbf{d} = (\sin\beta, \cos\beta)d$ where $\beta \in (0, 2\pi)$ is a uniform random angle and $d = d_\text{sample}\hat{\lambda}^{-1}$. We then construct ω_o using Eq. (30). The PDF of ω_o in this case is $p_s(d_\text{sample} \mid F_a)/P_s(d_\text{max} \mid F_a)$ divided by the Jacobian $|(d_\text{sample}, \beta) \to \omega_\text{o}| = z_\text{o}^{-1}\hat{\lambda}^{-2}d_\text{sample}$.

7.3. Refractive index

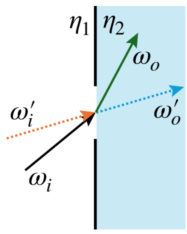

We handle the situation (see inset figure) where the front and back sides of the plane are in different media analogously to dielectric materials. If ω_i is the camera ray direction, we first calculate a (fake) refracted direction ω_o' (blue) using Sahl-Snell's law with the refractive indices of the two media. We then use ω_o' as the new incident direction ω_i' (orange) and sample (or evaluate the BSDF in) outgoing direction ω_o, with refractive index now set to that of the second medium $\eta = \eta_2$. For BSDF evaluation, this means we query the textures at $\mathbf{d} = \eta(\omega_\text{o} - \omega_\text{i}')_{xy}$ instead of $\mathbf{d} = (\omega_\text{o} - \omega_\text{i})_{xy}$.

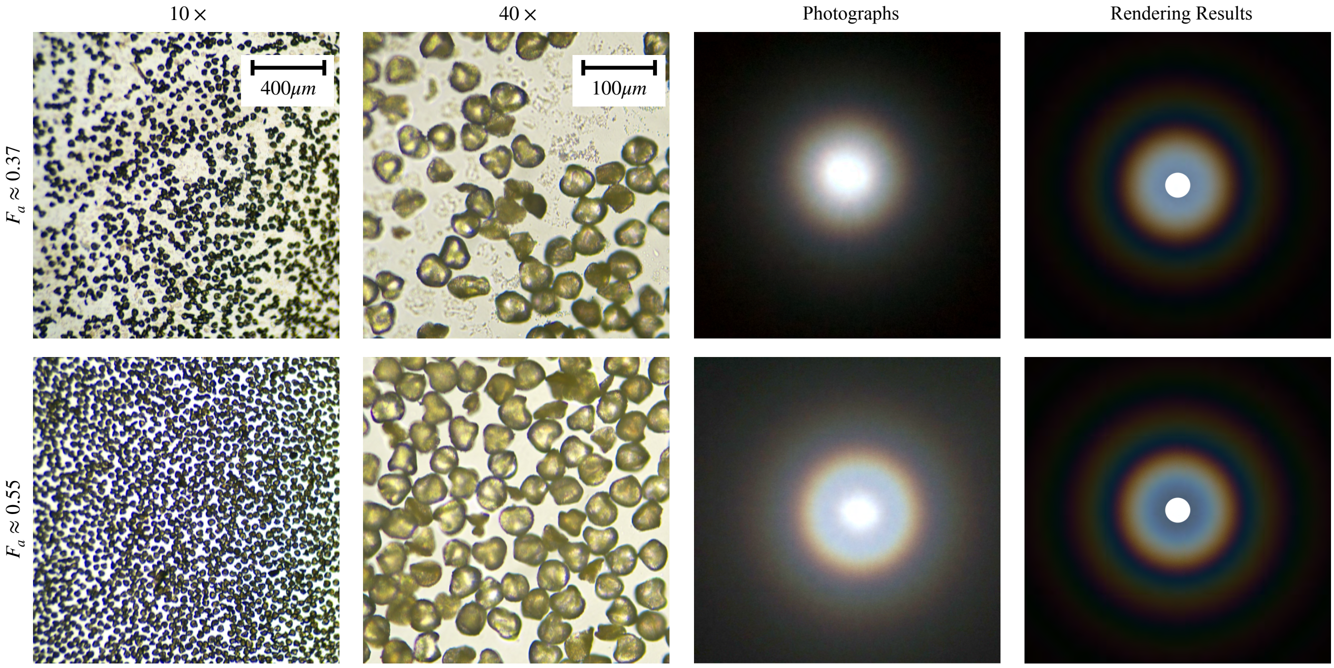

Figure 8: *Comparison of real-world and simulated corona effects for Lycopodium powder. The first two columns show microscope images which we binarize to estimate the area fraction F_a (top: ≈ 0.37, bottom: ≈ 0.55). The third column shows $4.25°$ field-of-view photographs of the powder illuminated by a small area light. The fourth column presents rendered images using our BSDF with matched parameters.*

The sampling process is analogous to how we previously queried texture values under different wavelengths. For reflection, the process is similar to refraction, but with $\eta = \eta_1$. This approach allows us to correctly account for the transition between media and ensures consistent behavior across the surface.

7.4. Spherical scatterers

Replacing apertures with spheres requires only two key changes. First, we replace Fraunhofer diffraction with Lorenz-Mie scattering, which depends on $(\omega_\mathrm{i} \cdot \omega_\mathrm{o})$ rather than $(\omega_\mathrm{o} - \omega_\mathrm{i})_{xy}$. This change reduces the problem to a 1D lookup table and requires us to evaluate additional Jacobian terms. Second, since the ratio between each component becomes more complex [GGB12], we store it in a separate 1D lookup table indexed by $(\omega_\mathrm{i})_z$.

8. Results

We built our BSDF model within Mitsuba 3 [JSR*22], and implemented several versions of our approach, including the on-the-fly product approach described in the previous section, and a baseline that pretabulates the product for specific parameter choices.

8.1. Variance reduction

When using on-the-fly products we can importance sample the BSDF by MISing the structure factor and aperture terms of the product. The baseline BSDF using pretabulated products can evaluate and importance sample according to the full product. Fig. 9 compares our method to this baseline and to naive cosine-weighted sampling

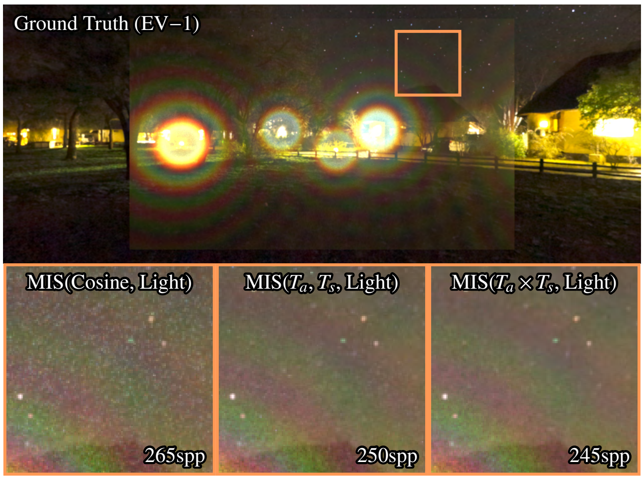

Figure 9: *We compare three different sampling approaches for our BSDF at equal time (25 s) to a high-spp ground truth (top). All methods perform MIS with emitter sampling but differ in how they evaluate and sample the BSDF component. Left: cosine-based sampling; Middle: MISing the aperture and structure factor textures as in Sec. 7; Right: evaluating and sampling the BSDF using a precomputed tabulation of the product.*

of the hemisphere that doesn't attempt to importance sample the BSDF at all. The results show that MISing the two terms is noisier than product sampling the combined BSDF, but our MIS version still substantially reduces variance compared to the cosine-based sampling baseline. All three methods combine with emitter sampling

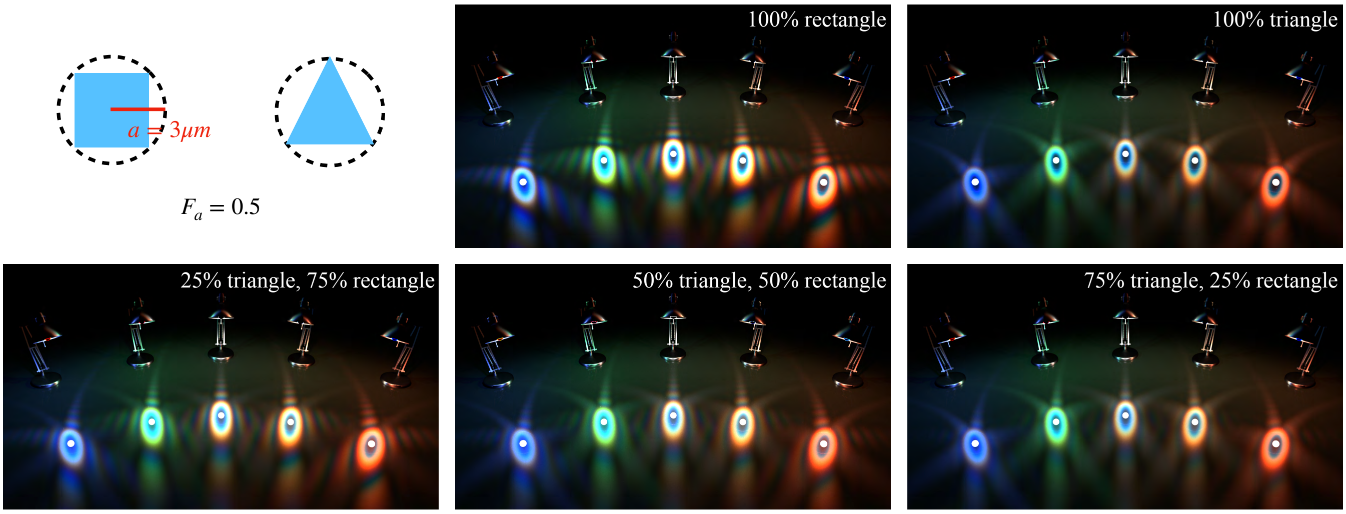

Figure 10: *Our model easily supports interpolating between different aperture shapes by controlling their mixing fraction. Here we smoothly transition between the four-sided interference pattern of square-shaped apertures to the six-sided symmetry of triangular ones.*

via MIS. Since all methods use tabulated BSDFs, the render times are roughly equal. In all the remaining results we compare converged renderings.

8.2. Real-world comparison with Lycopodium powder

Fig. 8 compares real-world observations with our rendered results. We take microscope images of Lycopodium powder and binarize them to estimate the area fraction F_a (top: ≈ 0.37, bottom: ≈ 0.55). We then photograph these two configurations back-lit by a small area light and render corresponding images using our BSDF with the estimated area fractions and similar scene parameters. As the area fraction increases, both the photographs and renderings exhibit more pronounced interference fringes. While some differences remain due to experimental factors, the overall structure and fringe spacing are consistent, demonstrating that our method captures the key diffraction features governed by area fraction and spatial arrangement.

8.3. Single aperture type

Fig. 14 summarizes how the diffraction pattern changes with aperture shape, size, area fraction, and surface orientation. Increasing the area fraction produces sharper, more pronounced interference fringes, while larger apertures focus energy more tightly at the center. The aperture shape directly imprints its symmetry onto the diffraction pattern, and tilting the surface causes directional stretching and asymmetry.

Our modular approach allows rendering all configurations using just four textures: one structure factor texture (shared across area fractions, as in Fig. 7) and three diffraction textures (circle, square, star). For a fixed aperture shape and size, higher area fractions yield more pronounced and sharper interference fringes.

Varying the surface orientation stretches the diffraction pattern because tilting reduces the in-plane projection of the wave vector difference, $\tilde{\mathbf{k}}$, even if the angle between incident and outgoing directions is unchanged. This leads to the observed asymmetry: the projection $\tilde{\mathbf{k}}$ varies with outgoing direction, causing direction-dependent distortions.

As the aperture radius increases, energy becomes more concentrated near the center of the diffraction pattern. This arises due to the inverse relationship between spatial and frequency scaling in the Fourier transform.

8.4. Mixed aperture types

In Fig. 10, we place five colored lamps on a surface with our BSDF to visualize diffraction patterns from a mixture of triangular and square apertures. Each shape produces a distinct pattern: triangles yield a hexagram due to their threefold symmetry, while squares create a four-pointed star. By gradually varying the shape ratio from 100% triangles to 100% squares, the overall diffraction transitions smoothly between these characteristic patterns. This demonstrates how aperture shape distribution directly affects the final diffraction appearance.

8.5. Spheres vs. Apertures

Fig. 11 compares the diffraction patterns produced by spherical scatterers and apertures, both with area fraction $F_a = 0.3$ and radius $a = 0.5\,\mu\text{m}$ (recall also the plots in Fig. 6). For each column, the incident plane is tilted by $0°$, $30°$, and $60°$, respectively. We observe that the patterns resulting from spherical scatterers are brighter (for aperture, there is more coherent component for larger F_a, but this is inverse for sphere) and also exhibit structural differences compared to those generated by apertures.

8.6. Scene rendering results

In Fig. 1 (bottom-right), we use our BSDF model to approximate condensation on a pair of glasses. We use a layer of circular apertures

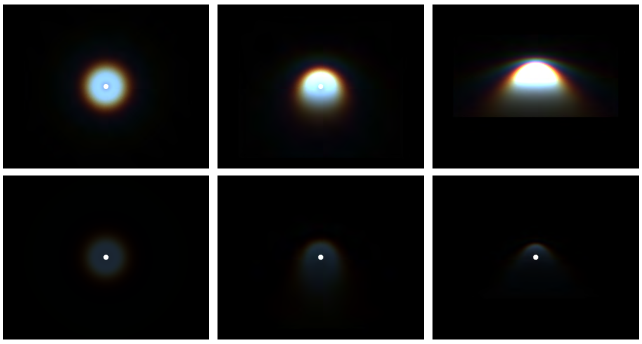

Figure 11: *The first row shows the diffraction patterns due to spherical scatterers, while the second row corresponds to those generated by apertures. Here, we use the area fraction $F_a = 0.3$. From left to right, the plane is tilted by $0°$, $30°$, and $60°$.*

(radius $a = 5\,\mu\text{m}$, area fraction $F_a = 0.5$) on a dielectric glass material with refractive index $\eta = 1.5$. This produces characteristic corona patterns around each light source due to diffraction and interference, which are also visible in reflections.

Fig. 12 also shows a glass material, but this time front-illuminated by two strong light sources that are reflected in the glass. While the corona is a forward-scattering phenomenon, interreflections and refractions between the two sides of the glass lead to a visible corona even in such front-illumination settings. Note that this is different than Quetelet scattering [XWM23], which models the interference *between* light reflected by a surface and scattering from fine particles near the surface. Our simulation does not compute interference as light travels between the front and back side of the glass.

Fig. 13 shows a curtain, where we use a rectangular elementary aperture and a diffuse BSDF f_r° for the parts that do not hit the diffraction holes. Here, the combination of aperture shape, occlusion, and varying orientations leads to rainbow-like diffraction effects.

9. Conclusion and discussion

We introduced a framework for modeling wave-optical scattering that accounts for both the shape of scatterers as well as their spatial correlations. Importantly, by keeping these concepts distinct, users can independently explore the visual impact of aperture shapes and spatial correlations without expensive recomputation.

For isotropic systems such as the hard disk model, a single structure factor texture suffices to represent a range of area fractions. We efficiently combine this texture with a precomputed single-aperture diffraction pattern (via FFT) to evaluate the BSDF. By adjusting the spatial frequency coordinate, we can scale the aperture without regenerating textures. Our importance sampling strategy leverages these two textures for efficient rendering. We further extended the framework to support mixtures of different aperture shapes and spherical scatterers.

9.1. Limitations and future work

Our method cannot pre-integrate over the spectral sensitivity function while maintaining the flexibility of combining aperture diffraction and structure factor textures. As a result, we rely on spectral rendering to capture wavelength-dependent effects. Using a small set of representative wavelengths (e.g., RGB) can mitigate this, but may miss subtle spectral interference.

Figure 12: *Corona effects from two strong light sources reflected and diffracted by a glass surface covered with circular apertures of radius $0.8\,\mu\text{m}$ and area fraction $F_a = 0.5$. The substrate is dielectric with refractive index 1.5. Both reflection and refraction contribute to the observed patterns.*

Figure 13: *A sheer curtain modeled as a layer of rectangular apertures with area fraction $F_a = 0.5$ on a diffuse substrate BSDF.*

Our current approach for a monolayer of spherical scatters introduces additional approximations. In contrast to apertures or discs, spheres are not flat, and the approximations we rely on [GGB12] do not fully account for multiple scattering or near-field interactions. In particular, this approximation can introduce errors at large scattering angles, where inter-particle interference becomes significant. Exploring more accurate models from optics might be a promising avenue for future work.

Our implementation is currently restricted to isotropic spatial relationships, where the PCF depends only on distance r, as in the hard disk system. However, the underlying theory naturally extends to anisotropic distributions, where the PCF depends on the full 2D vector $\mathbf{r}$. The same formulation applies, requiring only changes to texture generation and sampling.

PCFs can describe positional information in any dimension. Many natural systems—such as animal skins, bird feathers, or chameleon cells—exhibit particle distributions that are neither regular nor

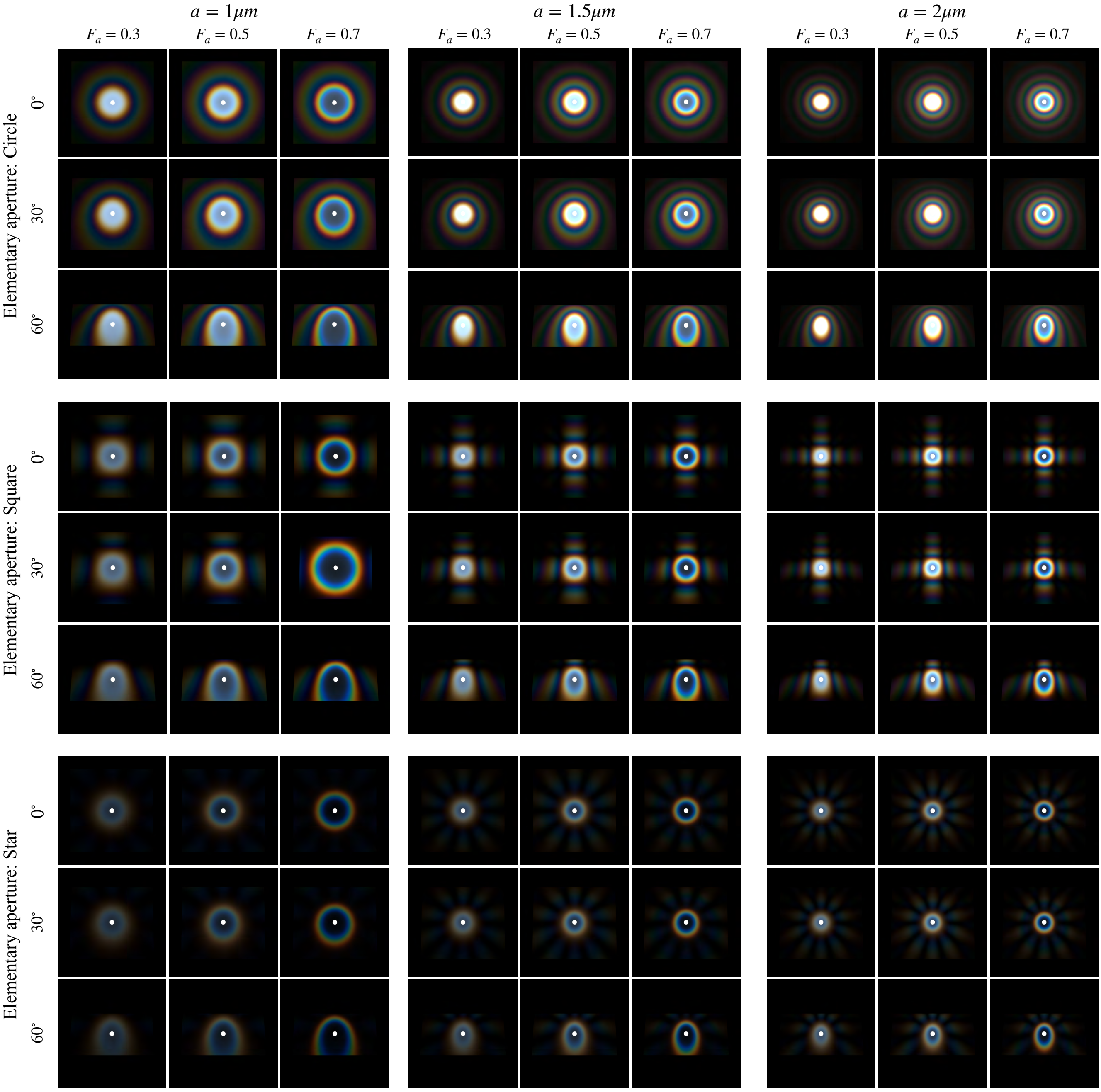

Figure 14: *Diffraction patterns produced by our BSDF model on a back-lit rectangular interface for various aperture configurations and viewing angles. The* 9×9 *grid is organized as* 3×3 *blocks, each corresponding to a specific aperture shape (rows: circle, square, star) and bounding circle radius (columns:* $a = 1\,\mu m$, $1.5\,\mu m$, $2\,\mu m$*). Within each block, columns represent different area fractions* ($F_a = 0.3, 0.5, 0.7$)*, and rows vary the plane orientation* ($30°, 60°, 90°$).

uniform. Prior work has addressed structured patterns like animal skin textures [DTS*14], but real-world scatterers often vary in size, spacing, or type. Anisotropic PCFs or full 3D PCFs could more accurately describe these complex scenarios. For example, chameleons modulate the spacing between nanocrystals in their skin to produce dynamic color changes—a phenomenon our framework could model using a spatially varying PCF.

10. Acknowledgments

We are grateful to the anonymous reviews for their suggestions on improving the paper. We also thank past and present members of the Dartmouth Visual Computing Lab, Kehan Xu for help during the deadline, Ziyuan Qu and Kedari Chowtoori for assisting with the powder experiment photos, Zihong Zhou for providing advice throughout the project, and Geoffrey Luke for agreeing to serve on the first author's MS thesis committee. This work was partially supported by NSF grant #1844538 and #2403122.

References

[AKV08] Adda-Bedia, M., Katzav, E., and Vella, D. "Solution of the Percus-Yevick equation for hard disks". *The Journal of Chemical Physics* 128.18 (May 14, 2008). issn: 0021-9606. doi: 10/d8jgx6 4.

[BB17] Belcour, L. and Barla, P. "A practical extension to microfacet theory for the modeling of varying iridescence". *ACM Transactions on Graphics (Proceedings of SIGGRAPH)* 36.4 (July 2017). issn: 0730-0301. doi: 10/dc3h 2.

[BH83] Bohren, C. F. and Huffman, D. R. *Absorption and Scattering of Light by Small Particles*. John Wiley & Sons, 1983. isbn: 978-0-471-29340-8 6.

[Bri49] Brillouin, L. "The scattering cross section of spheres for electromagnetic waves". *Journal of Applied Physics* 20.11 (Nov. 1, 1949). issn: 0021-8979. doi: 10/bgbccz 6.

[BSC11] Berg, M. J., Sorensen, C. M., and Chakrabarti, A. "A new explanation of the extinction paradox". *Journal of Quantitative Spectroscopy and Radiative Transfer*. Sixth International Symposium on Radiative Transfer 112.7 (May 1, 2011). issn: 0022-4073. doi: 10/bfswc8 6.

[CHB*12] Cuypers, T., Haber, T., Bekaert, P., Oh, S. B., and Raskar, R. "Reflectance model for diffraction". *ACM Transactions on Graphics* 31.5 (2012). doi: 10/gbbrp4 2.

[CLV05] Cowley, L., Laven, P., and Vollmer, M. "Rings around the sun and moon: coronae and diffraction". *Physics Education* 40.1 (Jan. 2005). issn: 0031-9120. doi: 10/djxz6p 2, 6.

[DTS*14] Dhillon, D. S., Teyssier, J., Single, M., Gaponenko, I., Milinkovitch, M. C., and Zwicker, M. "Interactive Diffraction from Biological Nanostructures". *Computer Graphics Forum* 33.8 (Dec. 2014). issn: 0167-7055, 1467-8659. doi: 10/f6q279 2, 6, 11.

[DW85] Dippé, M. A. Z. and Wold, E. H. "Antialiasing through stochastic sampling". *Computer Graphics (Proceedings of SIGGRAPH)* 19.3 (July 1, 1985). issn: 0097-8930. doi: 10/cmtt4s 3.

[FCJ07] Frisvad, J. R., Christensen, N. J., and Jensen, H. W. "Computing the scattering properties of participating media using Lorenz-Mie theory". *ACM Transactions on Graphics (Proceedings of SIGGRAPH)* 26.3 (July 29, 2007). issn: 07300301. doi: 10/bf3p26 2.

[GGB12] García-Valenzuela, A., Gutiérrez-Reyes, E., and Barrera, R. G. "Multiple-scattering model for the coherent reflection and transmission of light from a disordered monolayer of particles". *Journal of the Optical Society of America A* 29.6 (June 1, 2012). issn: 1520-8532. doi: 10/g867d6 2, 5, 6, 8, 10.

[GJZ21] Guo, Y., Jarabo, A., and Zhao, S. "Beyond Mie theory: Systematic computation of bulk scattering parameters based on microphysical wave optics". *ACM Transactions on Graphics (Proceedings of SIGGRAPH Asia)* 40.6 (Dec. 2021). doi: 10/kn59 2.

[Goo17] Goodman, J. W. *Introduction to Fourier Optics*. 4th ed. New York: W.H. Freeman, Macmillan Learning, 2017. 546 pp. isbn: 978-1-319-15304-5 3.

[HM13] Hansen, J.-P. and McDonald, I. R. *Theory of Simple Liquids: With Applications to Soft Matter*. 4th ed. Amsterdam: Academic Press, 2013. isbn: 978-0-12-387032-2 4.

[HSD13] Heck, D., Schlömer, T., and Deussen, O. "Blue noise sampling with controlled aliasing". *ACM Transactions on Graphics (Proceedings of SIGGRAPH)* 32.3 (July 2013). issn: 0730-0301. doi: 10/gbdcxt 4.

[HTSG91] He, X. D., Torrance, K. E., Sillion, F. X., and Greenberg, D. P. "A comprehensive physical model for light reflection". *Computer Graphics (Proceedings of SIGGRAPH)* 25.4 (July 1991). doi: 10/dsvjjq 2.

[IA00] Icart, I. and Arquès, D. "A physically-based BRDF model for multilayer systems with uncorrelated rough boundaries". *Rendering Techniques (Proceedings of the Eurographics Workshop on Rendering)*. Ed. by Péroche, B. and Rushmeier, H. Vienna: Springer, 2000. isbn: 978-3-7091-6303-0. doi: 10/g573xx 2.

[JSR*22] Jakob, W., Speierer, S., Roussel, N., Nimier-David, M., Vicini, D., Zeltner, T., Nicolet, B., Crespo, M., Leroy, V., and Zhang, Z. *Mitsuba 3 Renderer*. Version 3.0.1. 2022. url: https://mitsuba-renderer.org 8.

[LC94] Lock, J. A. and Chiu, C.-L. "Correlated light scattering by a dense distribution of condensation droplets on a window pane". *Applied Optics* 33.21 (July 20, 1994). issn: 2155-3165. doi: 10/cb482d 2, 3, 6.

[LD08] Lagae, A. and Dutré, P. "A comparison of methods for generating Poisson disk distributions". *Computer Graphics Forum* 27.1 (Mar. 1, 2008). issn: 0167-7055. doi: 10/cvqh4r 3, 4.

[LDI00] Loiko, V. A., Dick, V. P., and Ivanov, A. P. "Features in coherent transmittance of a monolayer of particles". *Journal of the Optical Society of America A* 17.11 (Nov. 1, 2000). issn: 1520-8532. doi: 10/cc44tg 2, 6.

[LML20] Loiko, N. A., Miskevich, A. A., and Loiko, V. A. "Scattering and absorption of light by a monolayer of spherical particles under oblique illumination". *Journal of Experimental and Theoretical Physics* 131.2 (Aug. 1, 2020). issn: 1090-6509. doi: 10/g867fb 2, 6.

[LML21] Loiko, N. A., Miskevich, A. A., and Loiko, V. A. "Polarization of light scattered by a two-dimensional array of dielectric spherical particles". *Journal of the Optical Society of America B* 38.9 (Sept. 1, 2021). issn: 1520-8540. doi: 10/gkc3br 6.

[Nay91] Nayar, S. K. "Surface reflection: physical and geometrical perspectives". *IEEE Transactions on Pattern Analysis and Machine Intelligence* 13.7 (July 31, 1991). doi: 10/b3hrqz 2.

[OKG*10] Oh, S. B., Kashyap, S., Garg, R., Chandran, S., and Raskar, R. "Rendering wave effects with augmented light field". *Computer Graphics Forum (Proceedings of Eurographics)* 29.2 (2010). issn: 1467-8659. doi: 10/c48wsg 2.

[PY58] Percus, J. K. and Yevick, G. J. "Analysis of classical statistical mechanics by means of collective coordinates". *Physical Review* 110.1 (Apr. 1, 1958). doi: 10/b4d735 4.

[Ros90] Rosenfeld, Y. "Free-energy model for the inhomogeneous hard-sphere fluid in D dimensions: Structure factors for the hard-disk (D=2) mixtures in simple explicit form". *Physical Review A* 42.10 (Nov. 1, 1990). doi: 10/bw252f 4, 5.

[SML*12] Sadeghi, I., Munoz, A., Laven, P., Jarosz, W., Seron, F. J., Gutierrez, D., and Jensen, H. W. "Physically-based simulation of rainbows". *ACM Transactions on Graphics* 31.1 (Jan. 2012). issn: 07300301. doi: 10/gfzndf 2.

[SÖA*19] Singh, G., Öztireli, C., Ahmed, A. G., Coeurjolly, D., Subr, K., Deussen, O., Ostromoukhov, V., Ramamoorthi, R., and Jarosz, W. "Analysis of sample correlations for Monte Carlo rendering". *Computer Graphics Forum (Proceedings of Eurographics State of the Art Reports)* 38.2 (Apr. 2019). doi: 10/gf6rzc 3.

[SRB*24] Steinberg, S., Ramamoorthi, R., Bitterli, B., Mollazainali, A., d'Eon, E., and Pharr, M. "A free-space diffraction BSDF". *ACM Transactions on Graphics (Proceedings of SIGGRAPH)* 43.4 (July 19, 2024). issn: 0730-0301. doi: 10/gt48vk 2.

[Sta99] Stam, J. "Diffraction shaders". *Annual Conference Series (Proceedings of SIGGRAPH)*. USA: ACM Press/Addison-Wesley Publishing Co., July 1, 1999. isbn: 978-0-201-48560-8. doi: 10/fv9fc4 2.

[TG17] Toisoul, A. and Ghosh, A. "Practical acquisition and rendering of diffraction effects in surface reflectance". *ACM Transactions on Graphics* 36.5 (July 2017). issn: 0730-0301. doi: 10/gcj3h7 2, 6.

[Uli87] Ulichney, R. *Digital Halftoning*. Cambridge, MA, USA: MIT Press, 1987. isbn: 0-262-21009-6 3.

[vdHul81] Van de Hulst, H. C. *Light Scattering by Small Particles*. NY: Dover Publications, 1981. isbn: 0-486-64228-3 2, 6.

[VG95] Veach, E. and Guibas, L. J. "Optimally combining sampling techniques for Monte Carlo rendering". *Annual Conference Series (Proceedings of SIGGRAPH)*. Vol. 29. ACM Press, Aug. 1995. isbn: 978-0-89791-701-8. doi: 10/d7b6n4 2.

[VWH18] Velinov, Z., Werner, S., and Hullin, M. B. "Real-Time Rendering of Wave-Optical Effects on Scratched Surfaces". *Computer Graphics Forum (Proceedings of Eurographics)* 37.2 (2018). issn: 1467-8659. doi: 10/gd2jnd 2.

[WVJH17] Werner, S., Velinov, Z., Jakob, W., and Hullin, M. B. "Scratch iridescence: Wave-optical rendering of diffractive surface structure". *ACM Transactions on Graphics (Proceedings of SIGGRAPH Asia)* 36.6 (Nov. 2017). issn: 0730-0301. doi: 10/ggfg4r 2.

[XWH*23] Xia, M., Walter, B., Hery, C., Maury, O., Michielssen, E., and Marschner, S. "A practical wave optics reflection model for hair and fur". *ACM Transactions on Graphics (Proceedings of SIGGRAPH)* 42.4 (July 26, 2023). issn: 0730-0301. doi: 10/gsk4gt 2.

[XWM*20] Xia, M., Walter, B., Michielssen, E., Bindel, D., and Marschner, S. "A wave optics based fiber scattering model". *ACM Transactions on Graphics (Proceedings of SIGGRAPH Asia)* 39.6 (Nov. 27, 2020). issn: 0730-0301. doi: 10/gsmm98 2.

[XWM23] Xia, M., Walter, B., and Marschner, S. "Iridescent water droplets beyond Mie scattering". *Computer Graphics Forum (Proceedings of the Eurographics Symposium on Rendering)* 42.4 (2023). issn: 1467-8659. doi: 10/gsk2rc 2, 10.

[YHW*18] Yan, L.-Q., Hašan, M., Walter, B., Marschner, S., and Ramamoorthi, R. "Rendering specular microgeometry with wave optics". *ACM Transactions on Graphics (Proceedings of SIGGRAPH)* 37.4 (July 2018). issn: 0730-0301. doi: 10/gd52td 2.

[YWW*24] Yu, Y., Weidlich, A., Walter, B., d'Eon, E., and Marschner, S. "Appearance modeling of iridescent feathers with diverse nanostructures". *ACM Transactions on Graphics (Proceedings of SIGGRAPH Asia)* 43.6 (Nov. 19, 2024). issn: 0730-0301. doi: 10/g9pgfm 2.

[YXW*23] Yu, Y., Xia, M., Walter, B., Michielssen, E., and Marschner, S. "A full-wave reference simulator for computing surface reflectance". *ACM Transactions on Graphics (Proceedings of SIGGRAPH)* 42.4 (July 26, 2023). issn: 0730-0301. doi: 10/gskz3f 2.